

# NO PLIF imaging in the CUBRC 48-inch shock tunnel

N. Jiang · J. Bruzzese · R. Patton · J. Sutton · R. Yentsch · D. V. Gaitonde ·  
W. R. Lempert · J. D. Miller · T. R. Meyer · R. Parker · T. Wadham ·  
M. Holden · P. M. Danehy

Received: 2 May 2012 / Revised: 22 August 2012 / Accepted: 29 August 2012 / Published online: 15 September 2012  
© Springer-Verlag 2012

**Abstract** Nitric oxide planar laser-induced fluorescence (NO PLIF) imaging is demonstrated at a 10-kHz repetition rate in the Calspan University at Buffalo Research Center's (CUBRC) 48-inch Mach 9 hypervelocity shock tunnel using a pulse burst laser-based high frame rate imaging system. Sequences of up to ten images are obtained internal to a supersonic combustor model, located within the shock tunnel, during a single  $\sim 10$ -millisecond duration run of the ground test facility. Comparison with a CFD simulation shows good overall qualitative agreement in the jet penetration and spreading observed with an average of forty individual PLIF images obtained during several facility runs.

## 1 Introduction

The need for optical diagnostic methods suitable for application in high-enthalpy hypervelocity short-duration facilities is especially acute due to the unique capabilities of these facilities for large-scale testing of hypersonic propulsion technologies at duplicated flight conditions as well

as the fundamental physics of hypervelocity flows. However, while the development of non-intrusive diagnostic techniques has experienced much recent progress, several challenges remain due to the inherent constraint of limited optical access and typically short (order 100's of microseconds to tens of milliseconds) steady state run times. Limitations on the number of facility "shots" per day (typically two to three in the current facility) are another consideration. Despite these challenges, several studies incorporating advanced optical diagnostic methods in such facilities have been recently reported. For example, nitric oxide molecular tagging velocimetry (NO MTV) (Danehy et al. 2009), Doppler-shift-based velocimetry (Danehy et al. 2001; Danehy and O'Byrne 1999), and NO planar laser-induced fluorescence (PLIF) measurements of number density and thermometry (O'Byrne et al. 2002) have been performed in the Australia National University's T2 free-piston shock tunnel. More recently, two-component Doppler-shift-based velocimetry has been demonstrated in the University of New South Wales' T-ADFA free-piston shock tunnel (Hruschka et al. 1996). As another example, a novel fuel plume imaging diagnostic, utilizing Mie scattering from in situ generated silica particles in combination with a long (100 microsecond)-pulsed Alexandrite laser, has been developed and applied to injector studies in the NASA-HYPULSE facility at General Applied Sciences Laboratory (GASL) (Tsai et al. 1996). NO number density measurements by UV absorption and NO PLIF have also been reported in the HYPULSE facility (Roberts et al. 1994). Several diagnostic advances have also been reported in studies at the Calspan University at Buffalo Research Center (CUBRC) LENS I and LENS II Hypersonic Shock Tunnels, including measurement of temperature and velocity by water vapor-based diode laser absorption (Wehe et al. 1988); NO number density, temperature and velocity

---

N. Jiang · J. Bruzzese · R. Patton · J. Sutton · R. Yentsch ·  
D. V. Gaitonde · W. R. Lempert (✉)  
Departments of Mechanical and Aerospace Engineering,  
The Ohio State University, Columbus, OH 43201, USA  
e-mail: lempert.1@osu.edu

J. D. Miller · T. R. Meyer  
Department of Mechanical Engineering, Iowa State University,  
Ames, IA 50011, USA

R. Parker · T. Wadham · M. Holden  
CUBRC, 4455 Genesee Street, Buffalo, NY 14225, USA

P. M. Danehy  
NASA Langley Research Center, Hampton, VA 23681, USA

Report Documentation Page			Form Approved OMB No. 0704-0188		
Public reporting burden for the collection of information is estimated to average 1 hour per response, including the time for reviewing instructions, searching existing data sources, gathering and maintaining the data needed, and completing and reviewing the collection of information. Send comments regarding this burden estimate or any other aspect of this collection of information, including suggestions for reducing this burden, to Washington Headquarters Services, Directorate for Information Operations and Reports, 1215 Jefferson Davis Highway, Suite 1204, Arlington VA 22202-4302. Respondents should be aware that notwithstanding any other provision of law, no person shall be subject to a penalty for failing to comply with a collection of information if it does not display a currently valid OMB control number.					
1. REPORT DATE <b>SEP 2012</b>		2. REPORT TYPE		3. DATES COVERED <b>00-00-2012 to 00-00-2012</b>	
4. TITLE AND SUBTITLE <b>NO PLIF imaging in the CUBRC 48-inch shock tunnel</b>			5a. CONTRACT NUMBER		
			5b. GRANT NUMBER		
			5c. PROGRAM ELEMENT NUMBER		
6. AUTHOR(S)			5d. PROJECT NUMBER		
			5e. TASK NUMBER		
			5f. WORK UNIT NUMBER		
7. PERFORMING ORGANIZATION NAME(S) AND ADDRESS(ES) <b>Ohio State University, Department of Mechanical and Aerospace Engineering, Columbus, OH, 43201</b>			8. PERFORMING ORGANIZATION REPORT NUMBER		
9. SPONSORING/MONITORING AGENCY NAME(S) AND ADDRESS(ES)			10. SPONSOR/MONITOR'S ACRONYM(S)		
			11. SPONSOR/MONITOR'S REPORT NUMBER(S)		
12. DISTRIBUTION/AVAILABILITY STATEMENT <b>Approved for public release; distribution unlimited</b>					
13. SUPPLEMENTARY NOTES					
14. ABSTRACT <b>Nitric oxide planar laser-induced fluorescence (NO PLIF) imaging is demonstrated at a 10-kHz repetition rate in the Calspan University at Buffalo Research Center's (CUBRC) 48-inch Mach 9 hypervelocity shock tunnel using a pulse burst laser-based high frame rate imaging system. Sequences of up to ten images are obtained internal to a supersonic combustor model, located within the shock tunnel during a single "10-millisecond duration run of the ground test facility. Comparison with a CFD simulation shows good overall qualitative agreement in the jet penetration and spreading observed with an average of forty individual PLIF images obtained during several facility runs.</b>					
15. SUBJECT TERMS					
16. SECURITY CLASSIFICATION OF:			17. LIMITATION OF ABSTRACT <b>Same as Report (SAR)</b>	18. NUMBER OF PAGES <b>10</b>	19a. NAME OF RESPONSIBLE PERSON
a. REPORT <b>unclassified</b>	b. ABSTRACT <b>unclassified</b>	c. THIS PAGE <b>unclassified</b>			

by NO-based diode laser absorption (Parker et al. 2006, 2007); and aero-optic distortion by Phase Shift Interferometry utilizing infrared scene generation and recording techniques (Holden et al. 1993; Holden and Parker 2002). Finally, Barker et al. (1998) have reported a novel flow tagging velocimetry diagnostic for use in high-enthalpy short-duration facilities based on laser-enhanced ionization of atomic sodium; Allen et al. (1993) have reported single-laser pulse NO PLIF-based thermometry in a high-enthalpy shock tunnel facility located at PSI corporation; and McMillan et al. (1993) have reported two-line NO PLIF temperature imaging of a transverse jet in a supersonic cross-flow. All of these imaging diagnostics have been performed with conventional  $\sim 10$ -Hz repetition rate pulsed laser sources, which limits data accumulation to one image per facility run.

More generally, since its inception more than twenty-five years ago (Dyer and Crosley 1982; Kychakoff et al. 1984), PLIF imaging has been developed into a powerful technique for qualitative and quantitative visualization in a wide variety of flow and combustion environments. However, the ability to capture unsteady flow dynamics at high speed is severely constrained by the relatively low repetition rates (order 10 Hz) of typical PLIF systems. Such instrumentation could only acquire a single image in one shock tunnel run. We have been developing, over the last several years, an ultra-high frame rate PLIF imaging system (up to 1 MHz frame rate) which combines a “burst mode” Nd:YAG-based tunable optical parametric oscillator (OPO) system (Jiang et al. 2008; Jiang and Lempert 2008) with a variety of high frame rate cameras, including CCD, ICCD and

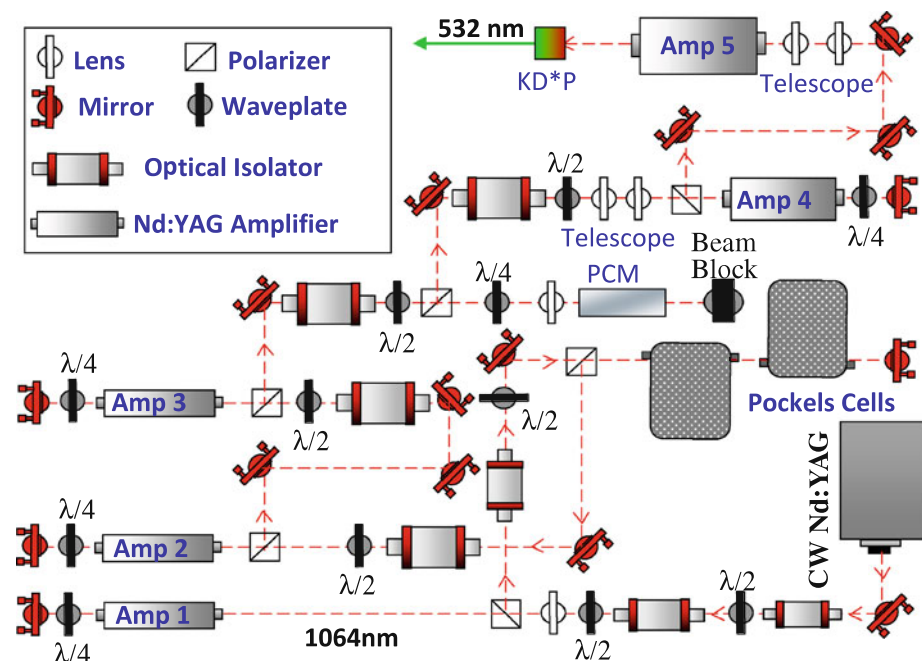
intensified CMOS architectures. In addition to enabling capture of the temporal dynamics of hypervelocity flows at frame rates up to 1 MHz, by operation at lower frame rates of the order of 10–20 kHz, the burst mode imaging system provides the unique ability to obtain sets of 8–10 full planar images in a single short-duration facility test. The work reported here was motivated by the desire to demonstrate such potential. Specifically, we demonstrate the ability to obtain ten high resolution NO PLIF images during a single run of the CUBRC 48-inch shock tunnel, operating at nominal Mach 9 free stream conditions. Images of injector plume mixing are obtained in a large-scale Multidisciplinary University Research Initiative (MURI) high-speed combustion duct in which NO-seeded helium is injected into a pure  $N_2$ -free stream. Comparison with a CFD simulation shows good overall agreement in fuel penetration and downstream spreading of the plume.

## 2 Experimental

### 2.1 Laser system description

The burst mode pump laser, illustrated in Fig. 1, has been described in detail previously (Jiang et al. 2009; Thurow et al. 2004) and will, therefore, be only summarized here. Briefly, a continuous wave (cw) diode-pumped Nd:YAG ring laser serves as the primary oscillator, the output of which is preamplified in a double-pass variable pulse width (from 0.3 to 2.0 ms) flashlamp-pumped pulsed amplifier. The amplifier rod is 10 cm in length by 6.4 mm in

**Fig. 1** Schematic diagram of five-amplifier configuration pulse burst Nd:YAG laser



diameter, and is wedged at a few degrees to mitigate self-lasing. The resulting preamplified output is formed into a “burst” train of short pulses using a custom, dual Pockels cell “slicer.” More specifically, the slicer produces burst sequences of 8–10 pulses at 1,064 nm, each with duration of  $\sim 10$  ns, and pulse energy of  $\sim 10^{-9}$  J (1 nJ). The series of pulses is further amplified in a series of four additional flashlamp-pumped amplifiers, with 6.4, 6.4, 9, and 12.7 mm diameter  $\times$  10-cm long rods, respectively. This configuration is somewhat different from the seven amplifier configuration which has been used previously for operation at burst frequencies of up to 1 MHz (Jiang et al. 2011). As will be discussed below, the desire to obtain the highest possible spatial resolution dictated the use of a 10-kHz frame rate-intensified CMOS camera, rather than the 1 MHz framing CCD camera used in most previous high-speed studies. The lower frame rate in turn dictated a correspondingly low (10 kHz) burst rate and corresponding burst envelope of 1 ms (10 pulses at 100 microsecond spacing). Due to very significant gain refilling between the individual pulses in the burst, only five amplifiers are required to reach the high energies required for these measurements. The remaining amplifier stages increase the individual average pulse energy from 1 nanoJoule to  $\sim 400$  mJ per pulse ( $4 \times 10^8$  gain) at 1,064 nm.

Note that amplifiers cannot simply be added arbitrarily, as system performance is ultimately limited by the growth of amplified spontaneous emission (ASE) in the forward direction. Inclusion of a stimulated Brillouin scattering (SBS) phase conjugate mirror (PCM) is a well-known approach for improving the spectral characteristics of a pulsed laser beam (Ni and Kung 1996). For this work, the purpose of the PCM is to both improve the on/off contrast of the pulse slicer and to limit ASE in the forward direction. Fluorinert FC-75, which has been used extensively as an SBS fluid (Jiang et al. 2008) and has previously performed well when operating the burst mode laser at less than  $\sim 250$  kHz (Jiang et al. 2008), was used for this work.

The fundamental output at 1,064 nm is converted to second- (532 nm) and third (355 nm)-harmonic wavelengths using a pair of KD\*P crystals. The third harmonic is then used as the pump for a home-built injection-seeded OPO system. The OPO output is sum-frequency mixed with residual 355 nm from the pump laser, creating high-frequency bursts of tunable output in the vicinity of 226 nm, which are used for NO PLIF imaging. The repetition rate of the burst sequence can be as high as 10 Hz, but is typically limited to 1–4 Hz when operating with burst envelopes exceeding  $\sim 0.5$  ms, due to thermal loading of the amplifier rods. Figure 2 shows a typical 10-pulse oscilloscope trace obtained at 10-kHz burst rate at 532 nm. The average individual pulse energy is  $\sim 150$  mJ. Note that the trace was obtained with a relatively low sampling rate

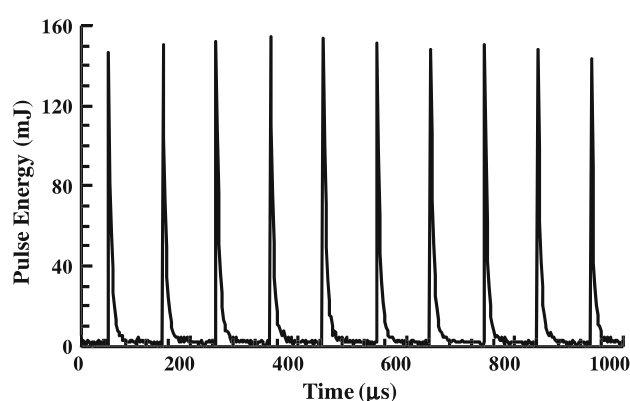


**Fig. 2** Typical ten-pulse laser burst trace at 532 nm with 100-microsecond inter-pulse spacing (10-kHz repetition rate). Average pulse energy is  $\sim 150$  mJ

oscilloscope that required the detector output to be deliberately broadened in time (using a load resistor and the intrinsic cable capacitance).

For spectrally narrowed imaging, the OPO was operated with injection seeding (Jiang et al. 2008) using an external cavity diode laser (ECDL) manufactured by Sacher, Inc. The OPO “idler” beam is seeded, which results in line-narrowed output for both the idler and signal waves, with time-averaged linewidth of  $\sim 300$  MHz, based on measurements using a commercial Fizeau wavemeter. For the seeded measurements performed in this work, the seed laser was tuned to 822.044 nm (vacuum wavelength), measured with a HighFinesse WS-6 Fizeau interferometer wavemeter. Mixing the output of the OPO with the third harmonic of the Nd:YAG laser produced UV output at 226.244 nm, exciting the  $Q_{11}(5.5) + QP_{21}(5.5)$  transition of the NO A–X (0,0) band (using the notation of Reisel et al. (1992)). The spectral linewidth at 226 nm, estimated from measurements of the linewidth of the 822 nm and 355 nm output, is  $\sim 0.5$  GHz, which is approximately equal to the NO pressure-broadened linewidth for static pressures of  $\sim 0.5$  bar and static temperatures of  $\sim 400$  K, which are typical values for the central portion of the imaged region of the flow (See Figs. 8, 9). This transition was selected based on the fact that the nominal static temperature of the fuel plume was predicted to vary between  $\sim 100$  K at the nozzle exit (i.e., the near wall region of the jet) and  $\sim 400$  K after mixing with the free stream flow. Figure 3 shows a set of 226-nm, 10 KHz burst traces. The average individual pulse energy is  $\sim 0.2$  mJ/pulse.

The UV beam had a circular cross-section with a 5 mm diameter, and it was directed upwards, using a series of mirrors, to the top of the facility. After propagation ( $\sim 5$  m) to the shock tunnel, however, the beam had diverged to  $\sim 10$  mm in diameter. The laser beam was then formed into a thin sheet using the combination of a cylindrical lens and a spherical lens. A positive 300-mm



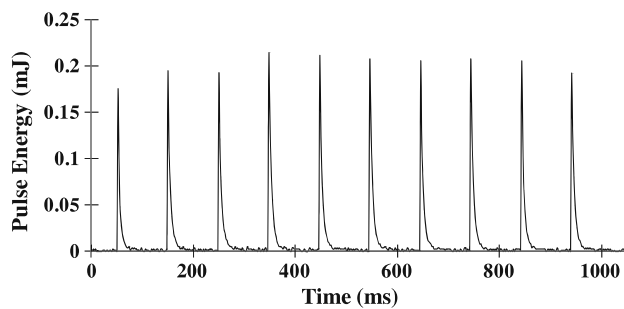


**Fig. 3** Typical ten-pulse laser burst trace at 226 nm with 100-microsecond inter-pulse spacing. Average pulse energy is  $\sim 0.2$  mJ

focal length cylindrical lens focused one axis of the beam which then propagated 600 mm and passed through a 1-meter focal length, 50-mm diameter spherical lens. This pair of lenses increased the total width of the beam to  $\sim 100$  mm. Of this 100 mm, the central 50 mm was used for the actual imaging. Using only the central portion resulted in improved sheet uniformity and also provided some accommodation to tunnel motion, which was known to translate parallel to the primary flow axis during facility operation. Since the beam delivery optics was not fixed with respect to the tunnel, this motion could, in principle, result in clipping of the sheet at the facility entrance window. In practice, this was not found to be a significant issue. The final UV laser sheet was  $\sim 0.6$  mm thick.

## 2.2 48-inch shock tunnel facility and pulse burst laser facility integration

The 48-inch shock tunnel facility is the smallest of three such hypersonic facilities located at CUBRC in Buffalo, N.Y., which can provide duplicated velocity/altitude conditions for combustion studies. Fundamental hypervelocity studies from high-enthalpy reentry physics to interceptor flow dynamics and turbulent combustion chemistry in full-scale combustion ducts have been studied with these facilities. The 48-inch shock tunnel can generate total enthalpy conditions in excess of 4 MJ/kg required for realistic temperature combustion studies at Mach 8. The steady state test times of 5–10 ms at this high-enthalpy condition provide sufficient flow lengths to stabilize complex interaction regions and the combusting flows behind angled wall jets in a flight scale (HiFiRE II) combustor. With different contoured nozzles and throats, the 48-inch shock tunnel can support test flows in the Mach number range from 6 to 20. For the proof of concept imaging experiments described in this work, a nominal Mach 9 nozzle/throat configuration was used to produce the pure nitrogen inlet test gas.

The MURI combustion duct is shown supported in the test section of the 48-inch shock tunnel in Fig. 5. This

combustion duct has dimensions of 40 cm (height)  $\times$  40 cm (span)  $\times$  200 cm (length). The rectangular combustion section within this model is approximately 10 cm (span)  $\times$  3 cm (height)  $\times$  30 cm in length where the Mach number is approximately 3 based on CFD computations. Five 0.254-cm diameter sonic fuel injectors are located on the bottom wall, spaced 6 mm apart and oriented at  $30^\circ$  with respect to the model floor. All five injectors are fueled. These injectors operate at an injection pressure of nominally 500 psi. For all images to be shown below, the injected gas is 5 % nitric oxide (NO) in helium, which is selected as a non-combustible surrogate for hydrogen, in order to study mixing.

The laser optical system is mounted on a portable optical table so that it could be employed in a number of different wind tunnel facilities. A separate portable cart was assembled for the flashlamp power supplies and other electrical driver components. The power supplies were individually fused to two standard three-phase 220-V, 30-amp breaker boxes. As illustrated schematically in Fig. 4, the UV output was directed through two fused silica windows, located at the top of the facility and test section, respectively. The downward propagating laser sheet was focused directly on the bottom surface of the combustor (there was no exit window). A 10 kHz intensifier (LaVision HS-IRO) and CMOS camera (Vision Research, Phantom 710) (as shown in Fig. 5) were placed close ( $\sim 150$  mm) to the test section imaging window, resulting in the object plane being approximately 0.75 m from the camera lens. The total camera pixel format was  $800 \times 1,200$ . As alluded to earlier, this camera was utilized in order to maximize obtainable spatial resolution while simultaneously maintaining an acceptable field of view. This camera was used in combination with a singlet plano-convex UV lens (200-mm nominal focal length, 50 mm diameter) for imaging. The resulting nominal object plane spatial scale was  $\sim 75$  microns/pixel, with actual spatial resolution limited in practice by the LaVision intensifier and the performance of the plano-convex lens. This imaging was accomplished using a nominal 1/3.4 magnification, resulting in a total object plane field of view of  $\sim 60$  mm (vertical)  $\times$  85 mm (horizontal) for the full  $800 \times 1,200$  pixel format sensor. Note that the intensifier diameter of 25 mm and the solid collection angle of  $\sim f/15$  were sufficient for high signal/noise instantaneous NO PLIF imaging.

Use of the available higher frame rate ICCD camera (Princeton Scientific Instruments, PSI-IV), which has a pixel format of  $160 \times 160$ , would have resulted in a spatial resolution degraded by a factor of approximately ten. Since it was initially estimated that the penetration of the injector plume into the free stream flow would in some cases be only on the order of 1–3 mm, it was decided to optimize maximum spatial resolution while limiting the frame rate to  $\sim 10$  kHz.

**Fig. 4** Simplified schematic diagram illustrating combustion duct and laser propagation geometry. Inlet flow is nominally Mach 9 and injection angle is approximately  $30^\circ$

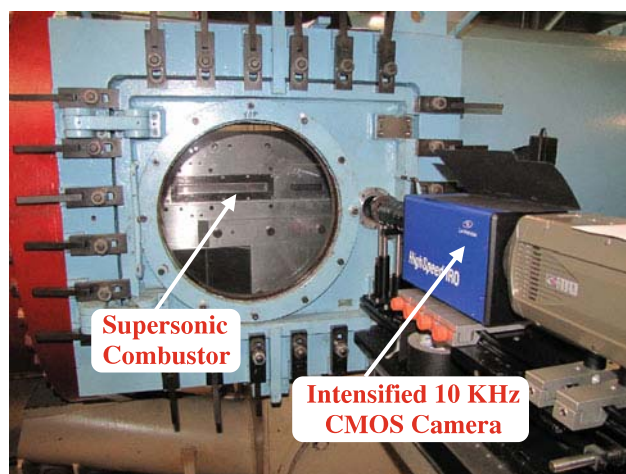
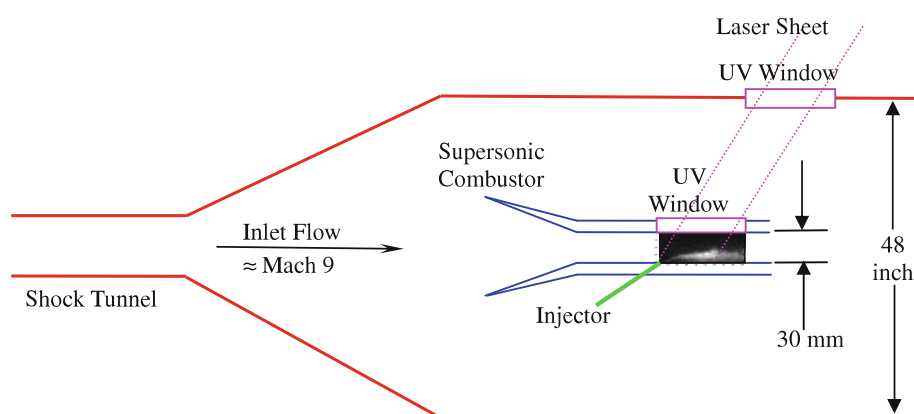


**Fig. 5** Photograph of generic scramjet engine model and intensified CMOS camera system

During the shock tunnel experiments, the intensifier gain was fixed at  $\sim 50\%$  of its maximum, and the exposure gate set to  $\sim 500$  ns. A custom-made 2-inch diameter transmission filter from Layertec, GmbH was placed in front of the plano-convex lens to attenuate the elastic laser scattering while transmitting most of the red-shifted fluorescence (transmit  $\ll 1\%$  @ 226 nm and  $>80\%$  @ 235–280 nm). This, in combination with applying black paint to the bottom surface of the combustor, was sufficient to eliminate stray elastic scattering from the laser sheet.

Due to the steady state test time of  $\sim 5$ – $10$  ms, a somewhat complicated scheme was required in order to synchronize the tunnel run with the laser and camera systems. In particular, the CMOS camera system required three distinct synchronization signals, and the pulse burst laser needed to be continuously triggered at 1 Hz during warm-up prior to the tunnel run, mostly due to the OPO and sum-frequency mixing crystals that were not temperature stabilized. The timing box labeled “SRS Delay Generator 1” (near the center of Fig. 6) was used to generate this 1 Hz system trigger. It triggered a second SRS delay

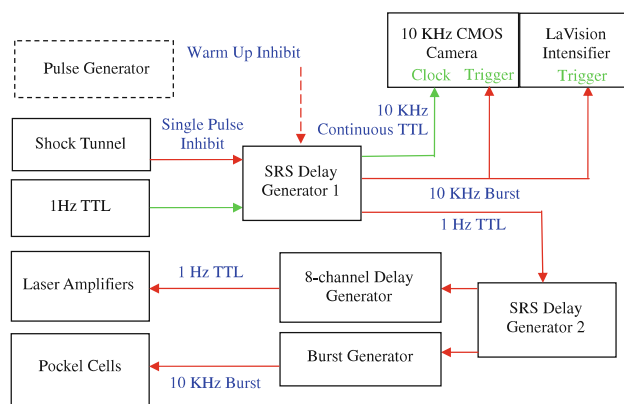


**Fig. 6** Block diagram illustrating triggering employed for shock tunnel measurements

generator, which in combination with two other delay generators provided triggers for the laser flashlamp power supplies and the pulse forming pulse slicer. This aspect of the synchronization/trigging was unchanged from our previous work. The Phantom CMOS camera required a continuous 10 kHz TTL “clock” pulse, as well as a separate 10 kHz burst for triggering the actual image acquisition series. The LaVision intensifier required a second 10 kHz burst for synchronization to the CMOS. The 10 kHz burst output of the primary SRS delay generator was inhibited with a 99.9 percent duty cycle (1 ms out of each 1 s cycle) during system warm-up (labeled “Warm Up Inhibit”). Just prior to a tunnel run, this inhibit timing was switched to a second timing box (labeled “Shock Tunnel”) which was triggered from a pressure transducer signal indicating that the primary flow had been established. In this manner, the 1-Hz warm-up was maintained for all but one pulse prior to the facility firing, and even this was manually manipulated to give a near 1-Hz interval between the warm-up trigger signals and that of the facility. Note that this procedure resulted in a maximum of  $\pm 50$  microsecond jitter between the triggering of the camera system and the start of acquisition, which is negligibly small compared to the facility run time of 5–10 ms.

### 3 Illustrative imaging results

#### 3.1 Prefacility run underexpanded jet images

In this section, we present a sampling of illustrative high-frequency frame rate imaging results at 10 kHz. Prior to obtaining images from shock tunnel runs, sets of images were obtained from the model in the identical geometry to that which would be used for tunnel runs but with the injector operating as a highly underexpanded jet (i.e., emptying into a nominal vacuum without a main flow). This provided a convenient means to align the optical system, determine adequate NO seed and intensifier gain levels, test the triggering and warm-up procedures, and also to provide an approximate assessment of the image quality. Figure 7 shows a typical six frame sequence of highly underexpanded jet images obtained from a single 10 kHz laser burst. The flow is NO/helium supplied through the five sonic orifices with a 500 psi plenum pressure. The laser sheet interrogates the flow out of a single orifice. The field of view is  $3.0\text{ cm} \times 6.5\text{ cm}$ , with corresponding spatial scale of  $\sim 75$  microns/pixel. The flow is propagating from bottom left to upper right, at an angle of  $\sim 45^\circ$ , with nozzle exit plane centered at the (x, y) location (1 cm,  $-0.5$  cm). While admittedly qualitative, the image quality is quite reasonable, illustrating the well-known, and rather complex, structure of the underexpanded jet. In particular, the characteristic “barrel” shock, with corresponding discontinuous increase in density, is clearly evident, as is some

irregular (possibly turbulent) structure, particularly downstream of the Mach disk (normal shock).

#### 3.2 Facility run images

Figure 8 shows an example eight-frame image sequence (top left to bottom right) obtained at 10-kHz frame rate from a single facility run at nominal free stream Mach number of 9. The field of view is again  $\sim 3.0\text{ cm} \times 6.5\text{ cm}$  and the nominal free stream flow velocity is  $\sim 1,200\text{ m/s}$ , with flow direction from left to right. The nominal static temperature and pressure at the exit of the fuel injector is  $\sim 100\text{ K}$  and  $\sim 140\text{ kPa}$ , respectively, based on a CFD simulation to be discussed in more detail below. The calculated free stream/jet exit momentum ratio, also based on CFD simulation, is 8.69. The corresponding conditions of the free stream flow directly upstream of the jet are  $\sim 530\text{ K}$  and  $30\text{ kPa}$ , respectively, so that in this instance, the jet is closer to pressure matched than for the images shown in Fig. 7. According to predictions of the CFD simulation, the injected jet initially expands, with static pressure dropping (due to mixing with the free stream) in the plume to  $\sim 10\text{--}20\text{ kPa}$ , followed by compression, due to the presence of a rather complex structure of oblique shocks, to  $\sim 50\text{ kPa}$ . There is an accompanying rise in static temperature to  $300\text{--}700\text{ K}$ , again according to CFD simulation.

The downward propagating laser sheet was brought incident to the facility from top right to bottom left, at an

**Fig. 7** Sequence of six underexpanded jet images from 5 % NO-seeded helium fuel injector, obtained from single laser burst at 10 kHz. Injector pressure is 500 psi, expanded into nominal vacuum. Imaged field of view is  $3.0\text{ cm} \times 6.5\text{ cm}$ . Laser sheet propagation direction is  $\sim 45^\circ$ , as indicated

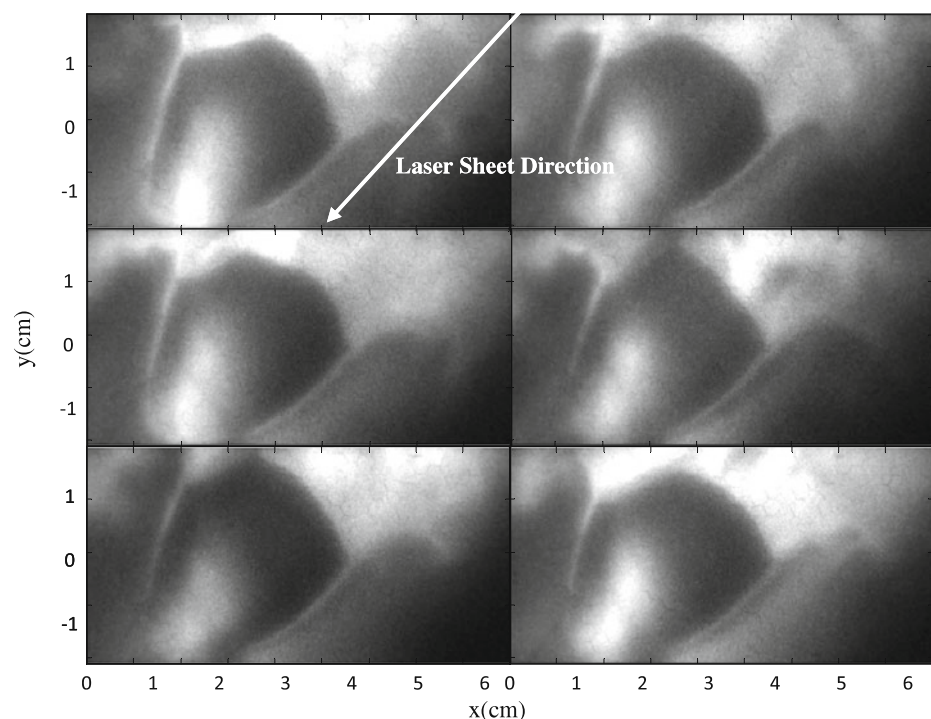
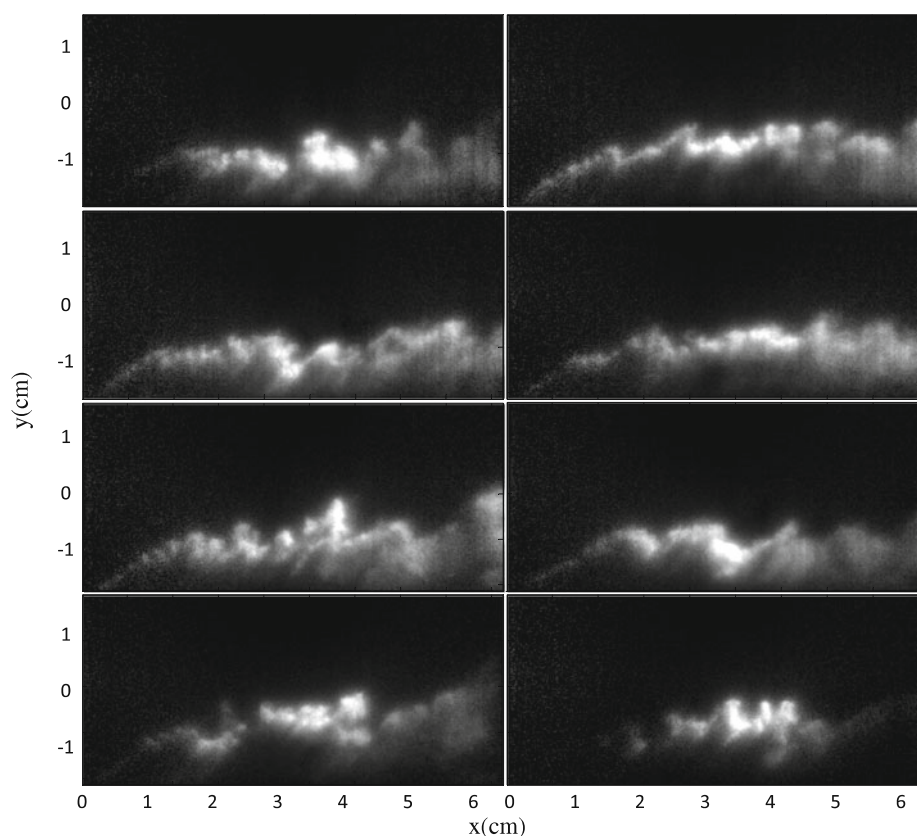




**Fig. 8** 10 KHz NO PLIF images of flow in supersonic combustor cavity. Injected gas is 5 % NO in helium at 500 psi pressure. Test gas is pure  $N_2$ . Injector angle is  $30^\circ$ . Field of view is  $\sim 3.0 \text{ cm} \times 6.5 \text{ cm}$



angle of  $\sim 45^\circ$ , as illustrated in Fig. 4. The gas is injected from the bottom-left corner at  $30^\circ$  injection angle with respect to the free stream flow direction. Note that the images shown in Fig. 7 have been cropped to display only  $\sim 400$  (height)  $\times$  900 (horizontal) pixels. The average intensity in detector “counts” is  $\sim 1,000$ – $3,000$  out of a total of 4,096, which was achieved using an intensifier gain of approximately  $\sim 50\%$  of its maximum. The corresponding background noise (mostly detector read noise) is  $\sim 20$  counts.

From Fig. 8, we can see that the fuel plume injection rapidly spreads and flaps, filling approximately half of the total 30-mm cavity height after only a few centimeters of downstream propagation. In actual operation, both floor and top injector banks would be utilized, which would result in a combustion chamber that is reasonably mixed at this point. It can be seen, however, that the mixing process is highly turbulent, as would be expected. While it cannot be determined definitively from planar imaging, it appears that the plume spreads rapidly, and turbulently, in three dimensions. Of course, since the flow speed is in excess of 1 km/sec, the images in Fig. 8 are temporally uncorrelated at the 10-kHz frame rate in which they were acquired. The uniformity of the laser sheet is also a potential issue when interpreting these images, but based on the images in Fig. 7, and recalling that the laser sheet is propagating

downward at  $\sim 45^\circ$ , it appears that, with the exception of the edges, sheet non-uniformity is not enormously significant. As stated previously, only the central two inches of a nominally four inch wide sheet was used for the actual imaging. In future experiments, it may be possible to measure the intensity distribution of the laser sheet on a pulse-to-pulse basis. This would be accomplished by use of an external dye cell and modification of the imaging system.

An underexpanded jet structure, similar to but much smaller than that shown in Fig. 7, was expected to be observed in Fig. 8, near the bottom-left side of each image. No such structure was observed. Three factors may contribute to prevent this structure from being observed. First, the laser intensity was likely considerably lower on the edges of the images (it also varies pulse-to-pulse, explaining some of the image-to-image and pulse burst-to-pulse burst variation). Second, high NO concentrations were probably absorbing the laser sheet energy, preventing fluorescence near the lower wall. Finally, it is possible that beam steering due to mechanical motion of the facility resulted in some clipping of the edges of the sheet, although it is noted that the beam was expanded considerably in an attempt to mitigate this. It is also noted that based on an approximate scaling (using a CFD simulation of the flow field to be discussed below) of measured



absorption in a room temperature gas cell filled with a mixture of 5 % NO in N<sub>2</sub>, we estimate that the laser beam absorption in the current experiment could be as high as 25 %/mm in the central portion of the image, corresponding to an absorption of  $\sim 75$  % over a uniform  $\sim 5$  mm “slab” of fluid. Clearly, this is a high level of absorption, and future NO PLIF measurements should be performed with lower seeding fraction. Finally, as will be described in more detail below, quenching, while significant in the jet core, is not sufficient to explain the lack of observed PLIF signal in that region.

Examining the fuel mixing in a time-averaged manner, the upper image in Fig. 9 is the average of 40 individual NO PLIF images obtained over several facility runs at the same flow condition. The nominal per pixel spatial scale is again  $\sim 75$  microns/pixel. From this image, it can be seen that the fuel penetrates the primary flow at the injection angle of  $\sim 30^\circ$ , propagates at  $30^\circ$  until it reaches approximately 7 mm in height above the floor, and then turns and propagates approximately parallel to the primary flow axis. At this point, the plume also spreads rapidly, due to turbulent diffusion. After approximately 2.5 inches (6.4 cm) of downstream propagation, the plume from the single floor injector has penetrated to just below the flow centerline.

A parallel computational effort was performed to aid in the interpretation and analysis of the experimental data. The bottom image in Fig. 9 is a CFD simulation obtained for the same flow condition as the NO PLIF average image. The simulation was performed using the GASP code from Aerosoft, Inc (2000). Although the actual experiment is highly unsteady, the steady state Reynolds-averaged Navier–Stokes (RANS) simulation performed provides an

“expected mean flow” baseline sufficient to aid in interpretation of data without the computational expense of a large-eddy simulation. The main features of jet are similar to those observed by Ben-Yakar et al. (2006) as well as by Gruber et al. (1995), including the Mach disk, bow shock, barrel shock, recirculation zones and counter rotating vortex pair, lending confidence to the accuracy of the overall simulation.

The structured, multi-block grid developed with the commercial Gridgen package consists of approximately 48 million cells and exploits symmetry by modeling only half of one injector row. For the simulation, a frozen-reaction chemistry model was developed from existing molecular thermodynamic profiles in GASP’s chemical database to predict viscous properties of the helium jet and nitrogen cross-flow. Given that the molar fractions of the NO seed are low in comparison with the other constituents, the effects of the NO are neglected in the gas model. The third-order upwind-biased Roe scheme is employed with a weighted essentially non-oscillatory limiter, giving an overall third-order accurate solution for inviscid fluxes. To simulate viscous effects, the Wilcox K-Omega model was used with a compressibility correction to account for over prediction of mixing in supersonic shear layers (Aerosoft Inc 2000). Turbulence trips were modeled using a forced intermittency transition along the walls as a feature of the turbulence model implementation in the GASP code.

To simulate the effects of finite sheet thickness, the computations shown in Fig. 9 (bottom) are composed of spatially averaged slices in the spanwise direction (in/out of plane of page). Specifically, the image represents the unweighted average of 12 infinitesimally thin slices, spaced 52-microns apart, a good match to the  $\sim 600$ -micron sheet thickness. This was deemed necessary as the simulation indicated a highly three-dimensional flow, with significant streamwise vorticity in the vortex pair arising downstream and complex accompanying wave and shock structure. The intensity scale is arbitrary and has been normalized to a peak value of one in the jet core.

For comparison purposes, the CFD simulation in Fig. 9 plots the relative PLIF signal,  $S_{PLIF}$  as follows:

$$S_{PLIF} \propto N_{tot} \chi_{NO} f_B QY \quad (1)$$

where  $N_{tot}$  is the total flow number density,  $\chi_{NO}$  is the NO mole fraction,  $f_B$  is the Boltzmann fraction for the excited quantum level, and  $QY$  is the fluorescence quantum yield, given by:

$$QY = \frac{A}{A + Q} \quad (2)$$

where  $A = 5 \times 10^6 \text{ s}^{-1}$  is the spontaneous radiative decay rate (Piper and Cowles 1986), and  $Q$  is the collisional quenching rate, given by:

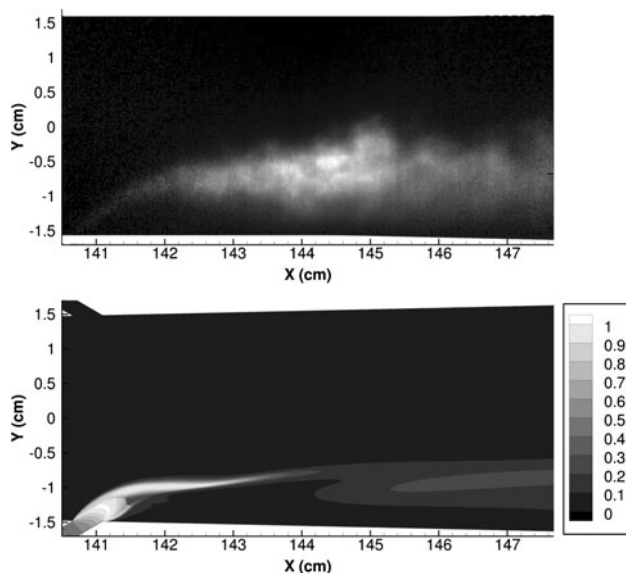


**Fig. 9** Comparison of averaged NO PLIF image with CFD simulation

$$Q(T) = 27.4 \times 10^{-11} N_{\text{tot}} \chi_{\text{NO}} \left( \frac{T}{300} \right)^{1/2} \quad (3)$$

Note that Eq. (3) assumes that the quenching by  $N_2$  and helium is negligible compared to NO–NO self-quenching, the rate for which at 300 K is taken from Paul et al. (1996). This is a reasonable assumption for  $\sim 95$  % of the mixing layer given the 5 % NO seeding level and given that NO has a quenching cross-section that is almost four orders of magnitude higher than that of  $N_2$ . Eq. (3) also assumes a temperature-independent quenching cross-section, as reported in reference (Paul et al. 1996), which results in the assumed  $T^{1/2}$  dependence in the quenching rate due to scaling by average molecular speed. Note that the quenching of the fluorescence in the core of the fuel jet attenuates the fluorescence signal in the core of the jet more than in the flow in the duct. Since the NO injection pressure is very high, the NO–NO quenching rate is also very high,  $\sim 8.1 \times 10^8 \text{ s}^{-1}$  at the  $\sim 140 \text{ kPa}$ , 100 K condition at the injector exit where  $\chi_{\text{NO}} \sim 0.05$ , and  $4.8 \times 10^7 \text{ s}^{-1}$  at center of the field of view of the jet, which has a static pressure and temperature (according to CFD) of  $\sim 37 \text{ kPa}$  and 500 K, respectively, and  $\chi_{\text{NO}}$  has dropped to  $\sim 0.025$  due to mixing with the free stream fluid. This should be compared to the NO radiative rate of  $\sim 5 \times 10^6 \text{ s}^{-1}$  ( $\sim 200 \text{ ns}$  lifetime) (Piper and Cowles 1986). Hence, the fluorescence quantum yield varies by a factor of approximately ten over the imaged region of the plume and is  $10 \times$  smaller in the plume than in the jet core.

While it is difficult to make an absolute comparison of the NO PLIF image, which has not been corrected for absorption and laser sheet non-uniformity, and the CFD simulation, it is clear that there is reasonable overall qualitative agreement. One significant discrepancy, noted above, is that the PLIF images do not show any indication of the barrel shock structure predicted by the CFD in the lower left region of the jet. As described above, the NO density is extremely high in this region and it is likely that absorption effects cause corresponding reductions in signal that mask the underexpanded jet structure. In future experiments, lower NO concentrations and weaker transitions could be used to reduce these complicating effects, thereby producing images that are easier to interpret. It also appears from this comparison that the simulation shows somewhat less spreading with distance downstream than the experimental data. This may be due to underprediction of turbulent mixing as well as the absence of large-scale unsteady structures in the computation; these trends are anticipated with the RANS approach. Finally, the CFD simulation predicts a thin region of high PLIF signal starting just downstream of the normal shock, where the jet fluid turns in the free stream direction, as well as a more complex structure in the downstream half of the image.

These features are manifestations of the rather complex, and three dimensional, structure of the jet, as predicted by CFD. Both of these predicted features are not observed in the experimental image, likely due to turbulent diffusion effects. The observed maximum intensity in the center of the image is almost certainly due to sheet non-uniformity, with maximum laser energy density in the center of the sheet.

## 4 Conclusions

Nitric oxide PLIF imaging has been demonstrated at 10-kHz repetition rate in the CUBRC 48-inch Mach 9 hypervelocity shock tunnel using a pulse burst laser system, a custom Optical Parametric Oscillator, and an intensified CMOS camera. During the run, 5 % NO in helium is injected into the combustor channel, providing a PLIF fuel tracer. Up to ten images of the jet mixing in the supersonic flow through the CUBRC MURI combustion duct were obtained during the 10-ms test time. High signal-to-noise images were obtained under typical free stream static temperature and pressure conditions of  $\sim 530 \text{ K}$  and 30 kPa, respectively, just upstream of the jet. Comparison with a CFD simulation shows, with some exceptions, good overall qualitative agreement of the predicted and observed penetration depth and spreading of the jet, based on averaging of over forty individual PLIF images obtained during several facility runs. This work demonstrates, for the first time, the capability of increasing the data rate of PLIF visualization methods in high-enthalpy impulse facilities by an order of magnitude utilizing burst mode laser technology. Future work will emphasize the capture of more quantitative flow properties.

**Acknowledgments** This work was supported by the Air Force Office of Scientific Research (John Schmisser—program monitor) and a NASA Phase I Small Business Innovative Research grant (Contract No. NNX10CE89P) to Spectral Energies, Inc. The Air Force Research Laboratory (James Gord) is also acknowledged for its ongoing contributions to the development of the laser technology essential to this work. The simulations have been performed on Department of Defense High-Performance Computing Modernization Program machines at AFRL and ERDC.

## References

- Aerosoft Inc, (2000) Kraft Drive, suite 1400 Blacksburg, VA 24060-6363, GASP Version 5.0 Reference Guide, February 2010
- Allen MG, Cronin JF, Davis SJ, Foutter RR, Parker TE, Reinecke WG, Sonnenfroh DM (1993) PLIF imaging measurements compared to model calculations in high-temperature mach 3 airflow over a sphere. AIAA Paper 93-0092
- Barker PF, Thomas AM, McIntyre TJ, Rubinsztajn-Dunlop H (1998) Velocimetry and thermometry of supersonic flow around a cylindrical body. AIAA J 36:1055–1060

- Ben-Yakar A, Mungal GM, Hanson RK (2006) Time evolution and mixing characteristics of hydrogen and ethylene transverse jets in supersonic cross flows. *Phys Fluids* 18:026101–026101-16
- Danehy PM, O'Byrne S (1999) Measurement of no density in a free-piston shock tunnel using PLIF. *AIAA Paper* 99-0772
- Danehy PM, Mere P, Gason MJ, O'Byrne S, Palma PC, Houwing AFP (2001) Fluorescence velocimetry of the hypersonic, separated flow over a cone. *AIAA J* 39:1320–1328
- Danehy PM, O'Byrne S, Houwing AFP, Fox JS, Smith DR (2009) Flow-tagging velocimetry for hypersonic flows using fluorescence of nitric oxide. *AIAA J* 41:263–271
- Dyer MJ, Crosley DR (1982) Two-dimensional imaging of OH laser-induced fluorescence in a flame. *Opt Lett* 7:382–384
- Gruber MR, Nejad AS, Chen TH, Dutton JC (1995) Mixing and penetration studies of sonic jets in a Mach 2 freestream. *J Prop Power* 11:315–323
- Holden M, Parker RA (2002) LENS hypervelocity tunnels and application to vehicle testing at duplicated flight conditions, Chapter 4. In: Lu F, Marren D (eds). *Advanced hypersonic test facilities*, vol. 198. American Institute of Aeronautics and Astronautics, Reston, VA
- Holden M, Craig J, Ratliff A, Sutton G (1993) Calibration and validation studies in the LENS facility. *AIAA Paper* 93-2682, June 1993
- Hruschka R, O'Byrne S, Kleine H (1996) Two-component Doppler-shift fluorescence velocimetry applied to a generic planetary entry probe model. *Exp Fluids* 48:1109–1120
- Jiang N, Lempert W (2008) Ultra-high frame rate nitric oxide planar laser Induced Fluorescence imaging. *Opt Lett* 33:2236–2238
- Jiang N, Lempert W, Switzer G, Meyer T, Gord J (2008) A narrow-linewidth MHz repetition-rate optical parametric oscillator for high-speed flow and combustion diagnostics. *Appl Opt* 47:64–71
- Jiang N, Webster M, Lempert W (2009) New advances in generation of high repetition rate burst mode laser output. *Appl Opt* 48:B23–B31
- Jiang N, Webster M, Lempert WR, Miller JD, Meyer TR, Ivey CB, Danehy PM (2011) MHz-Rate NO PLIF imaging in a mach 10 hypersonic wind tunnel. *Appl Opt* 50:A20–A28
- Kychakoff G, Knapp K, Howe RD, Hanson RK (1984) Flow visualization in combustion gases using nitric oxide fluorescence. *AIAA J* 22:153–154
- McMillan BK, Palmer JL, Hanson RK (1993) Temporally resolved, two-line fluorescence imaging of NO temperature in a transverse jet in a supersonic cross flow. *Appl Opt* 32:7532–7545
- Ni CK, Kung AH (1996) Effective suppression of amplified spontaneous emission by stimulated Brillouin scattering phase conjugation. *Opt Lett* 21:1673–1675
- O'Byrne S, Danehy PM, Houwing AFP (2002) Nonintrusive temperature and velocity measurements in a hypersonic nozzle flow. *AIAA Paper* 2002-2917
- Parker RA, Wakeman T, MacLean M, Holden M (2006) Nitric oxide concentration measurements with a quantum cascade laser in the LENS I hypersonic shock tunnel facility. *AIAA Paper* 2006-920
- Parker RA, Wakeman T, MacLean M, Holden M (2007) Measuring nitric oxide freestream velocity using a quantum cascade laser at CUBRC. *AIAA Paper* 2007-1329
- Paul PH, Gray JA, Durant JL, Thowman JW (1996) Collisional electronic quenching rates for NO  $A^2\Sigma^+$  ( $v' = 0$ ). *Chem Phys Lett* 259:508–514
- Piper LG, Cowles LM (1986) Einstein coefficients and transition moment variation for the NO ( $A^2\Sigma^+ - X^2\Pi$ ) transition. *J Chem Phys* 85:2419–2422
- Reisel JR, Carter CD, Laurendeau NM (1992) Einstein coefficients for rotational lines of the (0, 0) band of the NO  $A^2\Sigma^+ - X^2\Pi$  system. *J Quant Spectrosc Radiat Transf* 47:43–54
- Roberts WL, Allen MG, Howard RP, Wilson GJ, Trucco R (1994) Measurement and prediction of nitric oxide concentration in the HYPULSE expansion tube facility. *AIAA Paper* 94-2644
- Thurrow B, Jiang N, Samimy M, Lempert WR (2004) A narrow linewidth MHz rate pulse burst laser for high-speed flow diagnostics. *Appl Opt* 43:5064–5073
- Tsai C-Y, Callega JF, Bakos RJ, Rogers RC (1996) A technique for mixing measurement in hypervelocity pulse facilities using particle scattering imagery. *AIAA Paper* 96-2222
- Wehe SD, Baer DS, Hanson RK, Chadwisch KM (1988) Measurements of gas temperature and velocity in hypervelocity flows using a diode-laser absorption sensor. *AIAA Paper* 98-2699